

# Luminous type IIP SN 2013ej with high-velocity <sup>56</sup>Ni ejecta

V. P. Utrobin<sup>1,2★</sup> and N. N. Chugai<sup>3,4</sup>

<sup>1</sup>*Institute of Theoretical and Experimental Physics, B. Chermushkinskaya St. 25, 117218 Moscow, Russia*

<sup>2</sup>*Max-Planck-Institut für Astrophysik, Karl-Schwarzschild-Str. 1, 85748 Garching, Germany*

<sup>3</sup>*Institute of Astronomy, Russian Academy of Sciences, Pyatnitskaya St. 48, 119017 Moscow, Russia*

<sup>4</sup>*Sternberg Astronomical Institute, Moscow M.V. Lomonosov State University, Universitetskij pr., 13, 119234 Moscow, Russia*

Accepted XXX. Received YYY; in original form ZZZ

## ABSTRACT

We explore the well-observed type IIP SN 2013ej with peculiar luminosity evolution. It is found that the hydrodynamic model cannot reproduce in detail the bolometric luminosity at both the plateau and the radioactive tail. Yet the ejecta mass of  $23 - 26 M_{\odot}$  and the kinetic energy of  $(1.2 - 1.4) \times 10^{51}$  erg are determined rather confidently. We suggest that the controversy revealed in hydrodynamic simulations stems from the strong asphericity of the <sup>56</sup>Ni ejecta. An analysis of the asymmetric nebular H $\alpha$  line and of the peculiar radioactive tail made it possible to recover parameters of the asymmetric bipolar <sup>56</sup>Ni ejecta with the heavier jet residing in the rear hemisphere. The inferred <sup>56</sup>Ni mass is  $0.039 M_{\odot}$ , twice as large compared to a straightforward estimate from the bolometric luminosity at the early radioactive tail. The bulk of ejected <sup>56</sup>Ni has velocities in the range of  $4000 - 6500 \text{ km s}^{-1}$ . The linear polarization predicted by the model with the asymmetric ionization produced by bipolar <sup>56</sup>Ni ejecta is consistent with the observational value.

**Key words:** hydrodynamics – methods: numerical – supernovae: general – supernovae: individual: SN 2013ej

## 1 INTRODUCTION

The luminous type IIP supernova (SN IIP) 2013ej in M74 (Kim et al. 2013) gets into the limelight because of its early discovery, close location ( $D \approx 9 \text{ Mpc}$ ), and the unusual behavior. Specifically, at the plateau phase the flux declines more rapidly than normally in SNe IIP (Huang et al. 2015), which brought about a confusion with the classification of SN 2013ej, so one can meet type IIP (Huang et al. 2015), type IIP/IIL (Mauerhan et al. 2017), and type IIL (Bose et al. 2015) (below we prefer to use type IIP/L). Even more amazing is the luminosity evolution at the radioactive tail: decline at the early radioactive tail is more rapid than the <sup>56</sup>Co decay rate, which is a typical feature of SNe IIP (Dhungana et al. 2016). Moreover, the decline rate shows a slowdown after about 200 days instead of a decline acceleration. Yuan et al. (2016) attribute the rapid decline at the radioactive tail to either a low ejecta mass, a high explosion energy, an extreme outward mixing of <sup>56</sup>Ni, or a combination of these factors; the decline slowdown is not discussed. An interesting feature is the width and pronounced asymmetry of the nebular H $\alpha$  emission; the latter could indicate the bipolar <sup>56</sup>Ni ejecta (Bose et al. 2015) by analogy with SN 2004dj (Chugai et al. 2005). In this regard the detected

linear polarization at the level of  $\sim 1\%$  (Mauerhan et al. 2017; Kumar et al. 2016) is also reminiscent of SN 2004dj. The X-ray emission detected by *Chandra* and *Swift* indicates the mediocre wind density — characteristic of a red supergiant (RSG) (Chakraborti et al. 2016).

A good observational coverage of the light curve starting from the shock breakout and an extended set of spectra make SN 2013ej highly valuable object for the hydrodynamic modelling and the study of asymmetry effects in SNe IIP. Two hydrodynamic models for SN 2013ej have been reported (Huang et al. 2015; Morozova et al. 2017). However, both do not fit expansion velocities at the photosphere, which poses a question, whether supernova parameters are reliably inferred. The issue of adequate hydrodynamic parameters (ejecta mass, explosion energy, and pre-SN radius) therefore remains on the agenda. Note that both mentioned hydrodynamic models also do not touch the issue of the radioactive tail. The luminosity evolution at the radioactive tail, however, is closely related to the <sup>56</sup>Ni mass and mixing and therefore should be considered as a crucial observational constraint for the SN 2013ej model.

Here we address the issue of hydrodynamic parameters of SN 2013ej upon the basis of a standard one-dimensional (1D) hydrodynamic modelling of the bolometric light curve and expansion velocities. We also consider the problem of the <sup>56</sup>Ni distribution imprinted in the nebular H $\alpha$  profile

★ E-mail: utrobin@itep.ru

**Table 1.** Parameters of hydrodynamic models.

Model	$R_0$ ( $R_\odot$ )	$M_{ej}$ ( $M_\odot$ )	$E$ ( $10^{51}$ erg)	$M_{\text{Ni}}$ ( $M_\odot$ )	$v_{\text{Ni}}^{\text{max}}$ $\text{km s}^{-1}$
m23e1.2	1500	23.1	1.18	0.020	5000
m26e1.4	1500	26.1	1.40	0.039	6500

and in the luminosity decline rate at the radioactive tail. We start with the hydrodynamic modelling assuming different possibilities for the  $^{56}\text{Ni}$  mass and mixing (Section 2). We then consider an effect of the bipolar  $^{56}\text{Ni}$  jets on the nebular  $\text{H}\alpha$  profile and the radioactive tail (Section 3). The ejecta model and the recovered  $^{56}\text{Ni}$  distribution are used for the calculation of the polarization which in turn is compared to the observed polarization (Section 4). Results are summarized and discussed in Section 5.

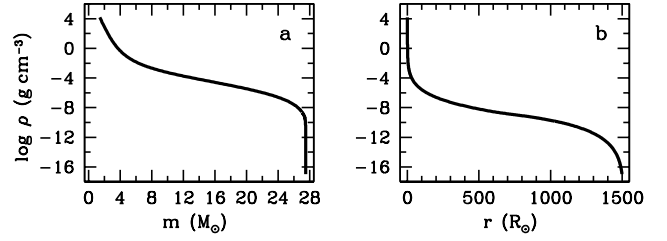
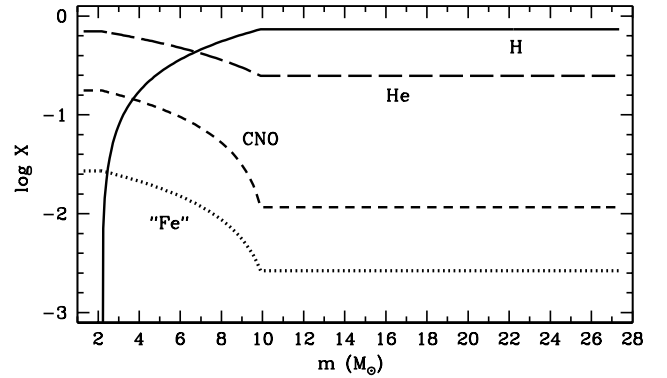
Below we adopt, following [Dhungana et al. \(2016\)](#), the distance to SN 2013ej  $D = 9.0$  Mpc and the reddening  $E(B - V) = 0.09$  mag.

## 2 HYDRODYNAMIC MODELLING

The light curve of SN 2013ej with a luminous plateau indicates that the pre-SN star was a red supergiant (RSG). Although at first glance it is advisable to explode a RSG model prepared by the evolutionary computations, the previous hydrodynamic simulations have demonstrated that the explosion of the evolutionary RSG is not able to describe all the essential features of the light curve ([Utrobin & Chugai 2008](#)). This problem in fact was first revealed for the peculiar type IIP SN 1987A. To produce sensible fit of the light curve, mixing at the He/H composition interface should be manually adjusted ([Woosley 1988](#)).

We therefore, as usually, choose a nonevolutionary hydrostatic RSG pre-SN model as the initial data for hydrodynamic simulation. A density profile and macroscopic mixing between metal, helium, and hydrogen components in such a model are adjusted to fit the photometric and spectroscopic data. Strictly speaking, the nonevolutionary model thus prepared is not a pre-SN in proper sense of this term. This model should be thought rather as an outcome of the Rayleigh-Taylor (RT) mixing caused by the shock propagation following the *explosion*. Yet for convenience we call this nonevolutionary model the “pre-SN”. Remarkably, recent three-dimensional (3D) simulations of the SN explosion of a RSG star show that the RT mixing modifies both the density and composition gradients at the composition interfaces in accord with the nonevolutionary pre-SN model used formerly in 1D simulations of the normal type IIP SN 1999em ([Utrobin et al. 2017](#)).

The explosion simulation of SN 2013ej utilizes the 1D hydrodynamic code with the radiation transfer ([Utrobin 2004](#)). The explosion is initiated by a supersonic piston applied to the bottom of the stellar envelope at the boundary with the collapsing  $1.4 M_\odot$  core. As a result of an extended simulations we come to alternative models m23e1.2 and m26e1.4 (Table 1) with two options of the  $^{56}\text{Ni}$  mass and mixing extent. The density and composition distributions in the pre-SN model m26e1.4 (called fiducial) are shown

**Figure 1.** Density distribution as a function of interior mass (Panel a) and radius (Panel b) for the pre-SN model m26e1.4. The central core of  $1.4 M_\odot$  is omitted.**Figure 2.** Mass fraction of hydrogen (solid line), helium (long dashed line), CNO elements (short dashed line), and Fe-peak elements excluding radioactive  $^{56}\text{Ni}$  (dotted line) in the ejecta of the pre-SN model m26e1.4.

in Figs. 1 and 2, respectively. The pre-SN model m23e1.2 has similar density and composition distributions except for  $^{56}\text{Ni}$ : here, unlike model m26e1.4, the  $^{56}\text{Ni}$  abundance is assumed constant by mass, which means that the  $^{56}\text{Ni}$  is center concentrated. In both models the pre-SN radius is  $1500 R_\odot$ , while the ejecta mass and the explosion energy are different.

The early detection of SN 2013ej provides an opportunity to verify the fiducial model m26e1.4 by comparing the calculated  $R$ -band light curve with the observations at the shock breakout stage (Fig. 3). The model  $R$ -band light curve fits the data fairly well including the first  $R$ -band observation of SN 2013ej ([Lee et al. 2013](#)) and the  $R$ -band photometry of [Dhungana et al. \(2016\)](#). Identifying the initial steep jump of the  $R$ -band light curve at the shock breakout with a non-photometric detection of SN 2013ej on July 24.125, which was reported by C. Feliciano on the Bright Supernovae website<sup>1</sup>, fixes the explosion at MJD=56494.705 (July 21.705), i.e., 2.195 days earlier compared to the estimate of [Dhungana et al. \(2016\)](#). We emphasize the difference between the explosion and shock breakout moments. Henceforth the SN age is counted from the adopted explosion moment. A low luminosity of the pre-SN model before the shock breakout at 2.42 days naturally accounts for the absence of a detectable emission on July 23.54 ([Shappee et al. 2013](#)).

Model m23e1.2 with the low amount ( $0.02 M_\odot$ ) and moderate mixing of radioactive  $^{56}\text{Ni}$  fits the bolometric light curve at the plateau stage (Fig. 4a), but fails at the radioac-

<sup>1</sup> <http://www.rochesterastromy.org/supernova.html>

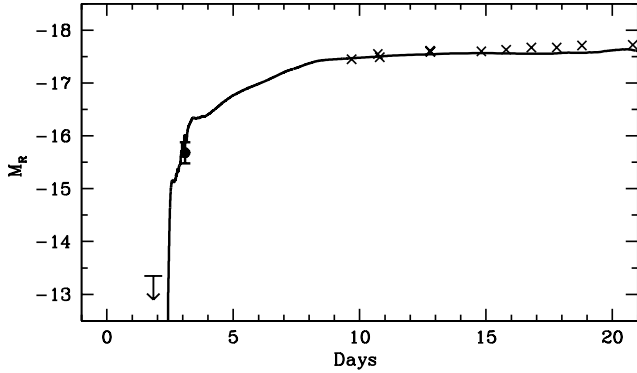


**Figure 3.** *R*-band light curve (solid line) during the first 20 days for the fiducial model m26e1.4. Arrow marks the upper limit  $V > 16.7$  for a non-detection on July 23.54 (Shappee et al. 2013), shown here for reference. Filled circle is the first observation of SN 2013ej in *R*-band with the uncertainty of about 0.2 mag announced by Lee et al. (2013). Crosses are the observational points of Dhungana et al. (2016). The time of the shock breakout of model m26e1.4 is identified with the epoch of the SN detection on July 24.125 reported by C. Feliciano.

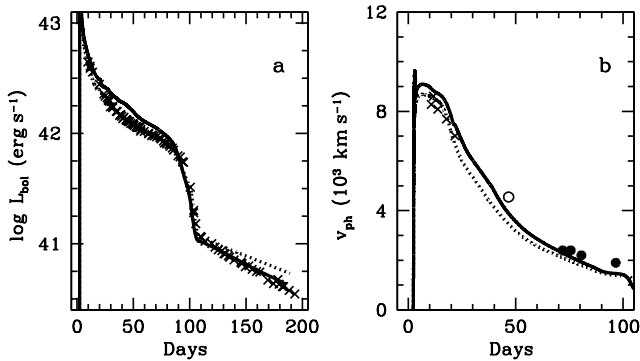


**Figure 4.** Hydrodynamic models m23e1.2 (dotted line) and m26e1.4 (solid line) for SN 2013ej. Panel a: the calculated bolometric light curves are overlotted on the bolometric data (crosses) reported by Dhungana et al. (2016). Panel b: the calculated photospheric velocity is compared with photospheric velocities estimated from the absorption minimum of the Si II 6355 Å line (crosses) by Dhungana et al. (2016) and recovered from the Na I doublet (open circle) and Fe II 6148 Å (filled circles) profiles.

tive tail where the calculated light curve declines slower compared to the observations. The latter is directly related to the deep location of  $^{56}\text{Ni}$ . The problem is solved in model m26e1.4 with the larger mass and more extended distribution  $^{56}\text{Ni}$  (Table 1). The radial distribution of  $^{56}\text{Ni}$  in this case (Fig. 5) is a spherical representation of the bipolar  $^{56}\text{Ni}$  jets, which are recovered below from the  $H\alpha$  line and the radioactive tail. Solving the problem of the radioactive tail, model m26e1.4, however, shows the 20% larger luminosity at the photospheric stage. The excess stems from the spherical distribution of  $^{56}\text{Ni}$  in the model, which ignores the fact that the bulk of  $^{56}\text{Ni}$  resides in the rear hemisphere (see Section 5). With these reservations model m26e1.4 is more preferred compared to m23e1.2.

Along with the bolometric light curve, the velocity at the photosphere level (photospheric velocity, for short) is

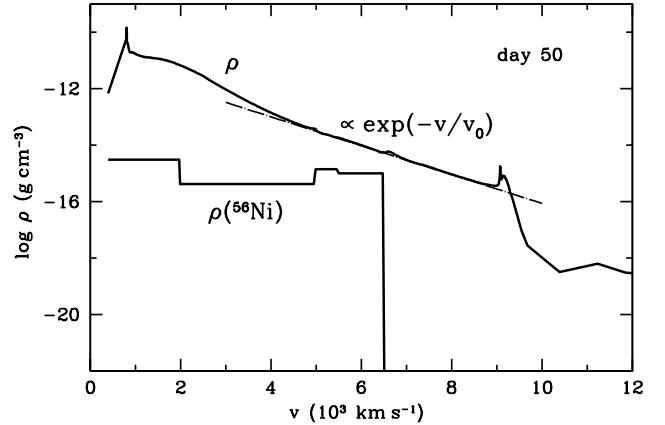


**Figure 5.** The gas and  $^{56}\text{Ni}$  density as a function of velocity for the fiducial model m26e1.4 at  $t = 50$  days (solid lines). Dash-dotted line is the exponential fit  $\exp(-v/v_0)$ .

another observable that should be met to constrain the hydrodynamic model. The photospheric velocity can be recovered from either absorption minima of weak metal lines or the profile modelling of stronger isolated lines. At the early phase we use the photospheric velocities obtained from Si II 6355 Å line (Dhungana et al. 2016). A photospheric velocity of  $4550 \text{ km s}^{-1}$  on day 44<sup>2</sup> is found using the Monte Carlo simulation of Na I 5890, 5896 Å doublet. Photospheric velocities of 2400, 2400, 2200, and  $1900 \text{ km s}^{-1}$  on days 69, 73, 78, and 94, respectively, were inferred from the Fe II 6148 Å line profile. The uncertainty of these velocity values does not exceed  $\pm 100 \text{ km s}^{-1}$ . Both hydrodynamic models reproduce the evolution of photospheric velocity (Fig. 4b) with a marginally better fit in the case of model m26e1.4.

### 3 NEBULAR $H\alpha$ LINE AND $^{56}\text{Ni}$ JETS

The broad appearance and pronounced asymmetry of the nebular  $H\alpha$  emission suggests that the ejecta likely harbors bipolar  $^{56}\text{Ni}$  ejecta (Bose et al. 2015) likewise in the type IIP SN 2004dj (Chugai et al. 2005). Here we explore this conjecture for SN 2013ej with the intention to infer parameters of the  $^{56}\text{Ni}$  distribution from the  $H\alpha$  profile and the radioactive tail of the bolometric light curve.

The exponential density distribution  $\rho \propto \exp(-v/v_0)$  is assumed for the ejecta mass of  $26 M_{\odot}$  and the kinetic energy of  $1.4 \times 10^{51}$  erg, in line with the fiducial model m26e1.4. Note that the exponential density distribution fits the results of hydrodynamic modelling (Fig. 5). The hydrogen abundance  $X = 0.7$  is assumed to be uniform throughout the ejecta. The  $^{56}\text{Ni}$  distribution is set by a central spherical component with the mass  $M_s$ , the outer velocity  $v_s$ , and the bipolar conical ejecta (jets) with the half-opening angle  $\psi$  and the inclination angle  $\theta$ ; in other respect the jets may be different. In the near hemisphere the jet (dubbed “blue jet”) contains  $M_b$  of  $^{56}\text{Ni}$  and lies in the velocity range  $v_{b1} < v < v_{b2}$ ; the “red jet” in the rear hemisphere contains  $M_r$  of  $^{56}\text{Ni}$  and lies in the velocity range  $v_{r1} < v < v_{r2}$ . The  $^{56}\text{Ni}$  density of each

<sup>2</sup> Hereafter the epochs of spectral observations are taken according to Dhungana et al. (2016)

component is assumed to be uniform to minimize a number of free parameters. The  $^{56}\text{Ni}$  presumably does not affect the background ejecta density.

Parameters of the  $^{56}\text{Ni}$  distribution are constrained by the two major observables: the nebular  $\text{H}\alpha$  profile and the luminosity evolution of the radioactive tail; both sets of data are taken from [Dhungana et al. \(2016\)](#). The distribution of the energy deposition throughout the ejecta is calculated in a single flight approximation for gamma-quanta with the absorption coefficient  $k_\gamma = 0.06Y_e$ , where  $Y_e$  is a number of electrons per nucleon ([Kozma & Fransson 1992](#)). Positrons from the  $^{56}\text{Co}$  decay presumably deposit their energy on-the-spot with the annihilation quanta taken into account in the gamma-ray emission of  $^{56}\text{Co}$  decay. The deposited energy is assumed to transform into radiation instantly. This approximation is valid until  $\sim 900$  days when a freeze out effect gets noticeable ([Fransson & Kozma 1993](#)). The  $\text{H}\alpha$  emissivity is assumed to be proportional to the local deposition rate  $\epsilon$ . This assumption is sufficient to obtain the  $\text{H}\alpha$  profile in relative fluxes. However, to take into account Thomson scattering effects in the emission profiles the distribution of electron concentration is also needed.

The local electron number density  $n_e$  can be determined from the ionization balance  $\epsilon/w = \alpha n_e^2$ , where  $w$  is the work per one hydrogen ionization, and  $\alpha$  is the recombination coefficient for upper levels  $n > 2$ , i.e., for the recombination case C, appropriate at the early nebular stage of SNe IIP; the electron temperature of 5000 K is assumed. The standard value  $w = 36$  eV was obtained for the collisional ionization losses of fast electrons in the hydrogen ([Dalgarno et al. 1999](#)). In SNe IIP a significant amount of deposited energy goes into the ultraviolet radiation that is able reionize hydrogen from the second level thus reducing the  $w$  value. One can use observational data of SN 1987A at the nebular epoch to infer a modified value of  $w$ . At the nebular stage, each hydrogen recombination creates one  $\text{H}\alpha$  photon, so if the  $\text{H}\alpha$  quanta escape, then the  $\text{H}\alpha$  luminosity is related to the bolometric luminosity as  $L(\text{H}\alpha) = (hv/w)L_{bol}$  (here  $hv$  is the energy of the  $\text{H}\alpha$  photon). This ratio is violated at the early nebular stage, when the  $\text{H}\alpha$  radiation is affected by an absorption. In SN 1987A the  $\text{H}\alpha$  is saturated at  $t < 200$  days which is indicated by the plateau in the  $\text{H}\alpha$  light curve during 150 – 200 days ([Hanuschik 1991](#)). On day 200, when the saturation effect becomes negligible, the SN 1987A  $\text{H}\alpha$  and bolometric luminosities suggest  $L(\text{H}\alpha) \approx 0.1L_{bol}$  ([Hanuschik 1991](#)), which in turn implies  $w \approx 20$  eV; this value is used below.

The optimal set of parameters of the  $^{56}\text{Ni}$  ejecta is given in Table 2. The  $\text{H}\alpha$  profile and the radioactive tail of the bolometric light curve are described fairly well with the found model of the bipolar  $^{56}\text{Ni}$  ejecta (Fig. 6). Remarkably, the model accounts for both the fast decline after day 110 and the slowdown of decline after day 200, the fact emphasized by [Dhungana et al. \(2016\)](#). In our search of the optimal parameters we bound ourselves with the requirement of the minimal  $^{56}\text{Ni}$  mass consistent with the  $\text{H}\alpha$  profile and the radioactive tail. The upper limit of the  $^{56}\text{Ni}$  mass cannot be reliably inferred by this kind of modelling because a high-velocity  $^{56}\text{Ni}$  ( $v > 7000$  km s $^{-1}$ ) does not affect significantly the  $\text{H}\alpha$  profile and the radioactive tail at the nebular stage.

**Table 2.** Parameters of  $^{56}\text{Ni}$  jets.

Parameter	Symbol	Value
Jets inclination	$\theta$	$56^\circ$
Half-opening angle	$\psi$	$30^\circ$
Mass of spherical component	$M_s$	$0.004 M_\odot$
Mass of blue jet	$M_b$	$0.011 M_\odot$
Mass of red jet	$M_r$	$0.024 M_\odot$
Velocity of spherical component	$v_s$	$2000$ km s $^{-1}$
Inner boundary of blue jet	$v_{b1}$	$2000$ km s $^{-1}$
Outer boundary of blue jet	$v_{b2}$	$5500$ km s $^{-1}$
Inner boundary of red jet	$v_{r1}$	$5000$ km s $^{-1}$
Outer boundary of red jet	$v_{r2}$	$6500$ km s $^{-1}$

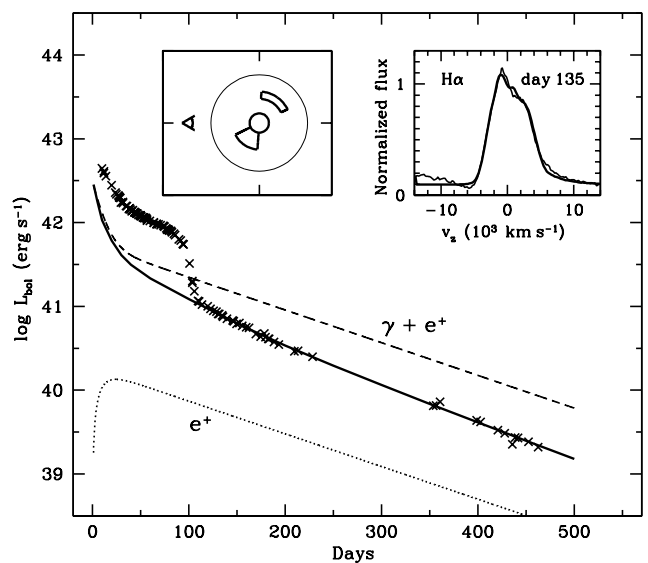


**Figure 6.** Bipolar  $^{56}\text{Ni}$  jet model (see Table 2) for the radioactive tail and the nebular  $\text{H}\alpha$  profile. *Solid line* is the model luminosity deposited by radioactive decay, *dashed line* is the total luminosity released by radioactive decay, *dotted line* is the power deposited by positrons, and crosses are the bolometric data reported by [Dhungana et al. \(2016\)](#). Inset in the left upper corner shows the model configuration of  $^{56}\text{Ni}$  components with respect to observer (on the left); the circle depicts the level in the ejecta at the velocity of  $10\,000$  km s $^{-1}$ . Right inset shows the calculated  $\text{H}\alpha$  (*thick solid line*) compared to that observed by [Dhungana et al.](#) on day 135 (*thin solid line*).

#### 4 $^{56}\text{Ni}$ JETS AND POLARIZATION

The aspherical ionization pattern produced by the  $^{56}\text{Ni}$  jets should result in the linear polarization due to the Thomson scattering likewise in SN 2004dj ([Chugai 2006](#)). The question arises, whether the polarization in our model is able to account for the observed polarization in SN 2013ej ([Mauerhan et al. 2017](#); [Kumar et al. 2016](#)). We consider only the nebular phase to minimize effects of the radiation transfer in the opaque ejecta. The polarization is calculated using the Monte Carlo technique ([Chugai 2006](#)). The model suggests that a quasi-continuum optical radiation is emitted with the rate proportional to the local deposition rate, the approximation valid at the nebular phase.

The computed polarization for the adopted ejecta and

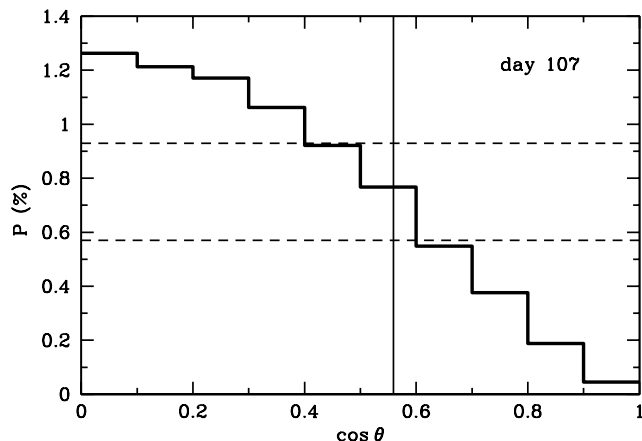


**Figure 7.** Linear polarization on day 107 as function of cosine of the jet inclination angle for the adopted model (*thick solid line*) (see Table 2). *Vertical line* marks the optimal inclination for the jet model, *dashed lines* show the observational range from two choices of interstellar polarization (Mauerhan et al. 2017).

the  $^{56}\text{Ni}$  jets model on day 107 is plotted in Fig. 7 as a function of the cosine of the inclination angle. For the optimal inclination angle  $\theta = 56^\circ$  the model polarization lies in the range between the observed polarization values obtained with alternative assumptions about the interstellar polarization (Mauerhan et al. 2017). The plot demonstrates that our model predicts the linear polarization consistent with the observational data. We conclude therefore that most (if not all) of the observed polarization seems to be related to the bipolar  $^{56}\text{Ni}$  ejecta.

A doubt may arise concerning the assumed collinearity of  $^{56}\text{Ni}$  jets. It may well be that the  $^{56}\text{Ni}$  ejecta could form as a result of the RT instability caused by the shock propagation (e.g. Wongwathanarat et al. 2015). In this case the opposite  $^{56}\text{Ni}$  ejecta generally are not collinear. Although our model of collinear jets agrees with the  $\text{H}\alpha$  and polarization data, we admit that this does not rule out the jets non-collinearity.

## 5 DISCUSSION AND CONCLUSIONS

Our aim has been to recover parameters of the hydrodynamic model for the unusual type IIP SN 2013ej and to explore the effects of a possible asymmetry of the  $^{56}\text{Ni}$  ejecta. We failed to find a unique spherical hydrodynamic model that would be able to fit well the light curve at both stages, the plateau and the radioactive tail. The model with  $0.02 M_\odot$  of the center-concentrated  $^{56}\text{Ni}$  describes the photospheric stage fairly well, but fails at the radioactive tail. The model with the twice as large amount of  $^{56}\text{Ni}$  residing at high velocities excellently fits the radioactive tail, but overproduces the luminosity at the plateau by a factor of  $\approx 1.2$ . Yet this model is preferred because the latter mismatch stems from the spherical representation of the bipolar  $^{56}\text{Ni}$  jets. In the real 3D picture with the bulk of radioactive  $^{56}\text{Ni}$  residing in the far hemisphere, the flux from the near hemisphere should be lower than in the spherical model due to the occultation effect. A correct description of the light curve

**Table 3.** Hydrodynamic models of type IIP supernovae.

SN	$R_0$ ( $R_\odot$ )	$M_{ej}$ ( $M_\odot$ )	$E$ ( $10^{51}$ erg)	$M_{\text{Ni}}$ ( $10^{-2} M_\odot$ )	$v_{\text{Ni}}^{\text{max}}$ ( $\text{km s}^{-1}$ )	$v_{\text{H}}^{\text{min}}$ ( $\text{km s}^{-1}$ )
1987A	35	18	1.5	7.65	3000	600
1999em	500	19	1.3	3.6	660	700
2000cb	35	22.3	4.4	8.3	8400	440
2003Z	230	14	0.245	0.63	535	360
2004et	1500	22.9	2.3	6.8	1000	300
2005cs	600	15.9	0.41	0.82	610	300
2008in	570	13.6	0.505	1.5	770	490
2009kf	2000	28.1	21.5	40.0	7700	410
2012A	715	13.1	0.525	1.16	710	400
2013ej	1500	26.1	1.4	3.9	6500	800

of SN 2013ej at the photospheric stage therefore requires a multi-dimensional radiation hydrodynamics.

The hydrodynamic modelling of SN 2013ej lead us to conclude that the ejecta mass is  $23.1 - 26.1 M_\odot$ , the explosion energy is  $(1.18 - 1.40) \times 10^{51}$  erg, the  $^{56}\text{Ni}$  mass is  $0.020 - 0.039 M_\odot$ , with the upper limits being preferred. The pre-SN should be a very extended RSG star with the radius of  $1500 R_\odot$ . The large pre-SN radius in our model is responsible for the luminous broad initial peak of the light curve. It is notable that the circumstellar (CS) shell with the radius of  $1300 - 1500 R_\odot$  and mass of  $\sim 1 M_\odot$  invoked by Morozova et al. (2017) can be considered as a proxy for our extended RSG model. Other SN parameters of both models cannot be meaningfully compared, because the information on the photospheric velocities in the model of Morozova et al. (2017) is lacking. Yet we note that our ejecta mass is twice as large.

It is instructive to confront the parameters of SN 2013ej with those of another luminous type IIP SN 2004et (Table 3). Both have similar ejecta masses and pre-SN radii. However, the explosion energy and the  $^{56}\text{Ni}$  mass of SN 2013ej are by a factor of  $\sim 1.6$  lower than those of SN 2004et. Moreover, the maximal velocities of  $^{56}\text{Ni}$  are dramatically different:  $1000 \text{ km s}^{-1}$  in SN 2004et vs.  $6500 \text{ km s}^{-1}$  in SN 2013ej. This disparity indicates that the explosion outcome in SNe IIP can be significantly different even for comparable pre-SN masses.

An intriguing point is the physics behind the steep decline of the light curve of SN 2013ej at the photospheric stage. While the initial broad luminosity peak postpones the cooling and recombination wave regime, this does not explain the lack of the flat plateau at the later photospheric stage. In contrast, SN 2004et after about day 35 shows a *flat* plateau (Sahu et al. 2006). The reason for the different behavior of SN 2013ej at this stage is hidden in the density distribution of a pre-SN model. Specifically, at the transition between the helium core and the hydrogen envelope the density gradient in the pre-SN model of SN 2013ej varies with the radius more smoothly compared to that of SN 2004et. We attribute this distinction to the different outcome of the RT mixing during the explosion, viz., in SN 2013ej mixing was more vigorous than in SN 2004et. This conjecture seems to be supported by the low velocities of the  $^{56}\text{Ni}$  matter in SN 2004et ( $v_{\text{Ni}}^{\text{max}} = 1000 \text{ km s}^{-1}$ ) and the high  $^{56}\text{Ni}$  velocities in SN 2013ej ( $v_{\text{Ni}}^{\text{max}} = 6500 \text{ km s}^{-1}$ ). Whether the proposed

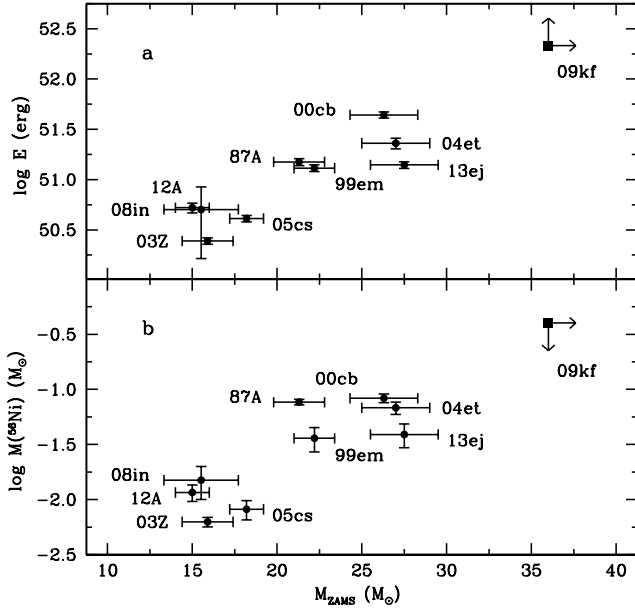


**Figure 8.** Explosion energy (Panel a) and  $^{56}\text{Ni}$  mass (Panel b) vs. hydrodynamic progenitor mass for SN 2013ej and nine other core-collapse SNe (Utrobin & Chugai 2015).

explanation of SN IIP/L phenomena is universal remains to be verified.

Combining the SN 2013ej ejecta mass with a neutron star of  $1.4 M_{\odot}$  and a moderate mass of  $1 - 2 M_{\odot}$  lost by the stellar wind (cf. Utrobin & Chugai 2009), one comes to the progenitor mass of  $25.5 - 29.5 M_{\odot}$ . The parameters of our fiducial model m26e1.4 on the diagrams of the explosion energy vs. the progenitor mass and the  $^{56}\text{Ni}$  mass vs. the progenitor mass (Fig. 8) place SN 2013ej into the high mass region at the lower boundary of both scatter plots. Now the sample of well-observed SNe IIP studied hydrodynamically in a uniform way (Utrobin & Chugai 2015) mounts up to ten and this reinforces our former impression that the SN IIP mass distribution is skewed towards high masses with an apparent deficit of SNe IIP in the range of  $9 - 15 M_{\odot}$ . This in turn brings about a tension with general wisdom that stars with the main-sequence masses of  $9 - 25 M_{\odot}$  produce SNe II. The tension is alleviated, if one admits that that SNe from the mass range of  $9 - 15 M_{\odot}$  are very faint, so they escape detection. This serious issue requires a further thorough study.

The model of extended asymmetric  $^{56}\text{Ni}$  ejecta of SN 2013ej is found to be compatible with the polarization data at the early nebular epoch. Mauerhan et al. (2017) suggest that the Thomson scattering in an oblate ellipsoidal envelope and the dust scattering in the CS envelope could be responsible for the polarization in SN 2013ej. In this regard we notice that the mechanism of the asymmetric ionization related to the CS interaction invoked by Mauerhan et al. (2017), cannot noticeably modify the asymmetry produced by the bipolar  $^{56}\text{Ni}$  ejecta. Indeed, the X-ray luminosity associated with the CS interaction on day 114 is three orders lower than the bolometric luminosity at the same epoch (cf. Chakraborti et al. 2016).

The bipolar structure of  $^{56}\text{Ni}$  in SN 2013ej is reminiscent of SN 2004dj (Chugai et al. 2005) with an exception

that the  $^{56}\text{Ni}$  amount in SN 2013ej is twice as large and the maximal velocity of  $^{56}\text{Ni}$  is also a factor of two larger. The high velocity of the  $^{56}\text{Ni}$  ejecta in SN 2013ej is a challenge for the explosion mechanism. In the neutrino-driven explosion mechanism, high velocities of the  $^{56}\text{Ni}$ -rich matter in SNe IIP are explained as an outcome of the RT instability that accompanies the shock wave propagation in the inner parts of the exploding star. Recent 3D simulations of an explosion of a  $15 M_{\odot}$  RSG model demonstrate that the RT plumes of  $^{56}\text{Ni}$  are able to protrude up to  $4000 - 5000 \text{ km s}^{-1}$  (Wongwathanarat et al. 2015). However, the simulations show also that in a more massive star of  $20 M_{\odot}$  the  $^{56}\text{Ni}$  velocities are a factor of 1.5 lower. Thus, at the moment it is not clear, whether the RT mechanism is able to account for the  $^{56}\text{Ni}$  velocities of  $\sim 6000 \text{ km s}^{-1}$  in SNe with the mass of  $\sim 25 M_{\odot}$ . It is noteworthy that the velocity extent of  $^{56}\text{Ni}$  in SN 2013ej is not extreme among SNe IIP: in SN 2000cb the  $^{56}\text{Ni}$  matter seems to be mixed up to  $8400 \text{ km s}^{-1}$  (Utrobin & Chugai 2011). In this regard it may well be that apart from the RT mixing some additional asymmetry of the explosion could be involved in the buildup of high velocities of  $^{56}\text{Ni}$ . One way or another, the asymmetry and high velocities of the  $^{56}\text{Ni}$  ejecta in SNe IIP should be considered as crucial observational constraints for the explosion mechanism. Finally, note that the bipolar high-velocity  $^{56}\text{Ni}$  ejecta in SN 2013ej is not unique phenomenon: the well-known high-velocity bipolar jets in Cas A (SN IIf) are the firmly established feature that apparently has an explosion origin (Fesen & Milisavljevic 2016).

For SN 2013ej our estimate of the progenitor mass (dubbed “hydrodynamic mass”) is significantly larger than  $8 - 15.5 M_{\odot}$  (dubbed “pre-SN luminosity mass”) inferred from pre-explosion *HST* F814W-filter image (Fraser et al. 2014). The SN IIP progenitor mass problem was recovered and discussed first in the context of SN 2005cs (Utrobin & Chugai 2008), in which case hydrodynamic mass turned out to be significantly larger than the ZAMS mass from archival image (Maund et al. 2005). Since then the mass problem is reproduced *every time* when both mass estimates are available. The exception is SN 1987A, for which both methods provide similar mass estimates of  $\sim 20 M_{\odot}$ . This in turn indicates that the mass problem arises possibly only in cases when the SN IIP event is related to the RSG explosion.

The conflict between hydrodynamic and pre-SN luminosity masses suggests that either the former or latter method is in error. Our hydrodynamic code in case of SN 1999em — classic SN IIP — produces similar SN parameter values (Utrobin 2007) to those obtained by independent codes of Baklanov et al. (2005) and Bersten et al. (2011). It should be emphasized that the codes use different treatment of radiation transport: one-group radiation transfer (Utrobin 2007), multi-group radiation transfer (Baklanov et al. 2005), and flux-limited equilibrium diffusion approximation (Bersten et al. 2011). This indicates the robustness of the recovered parameter values provided that the observables (bolometric light curve and photospheric velocities) are adequately modeled. It should be highlighted that in some cases hydrodynamic studies of SNe IIP are limited to the light curve modelling, ignoring photospheric velocities. In this approach the ejecta mass and the explosion energy cannot be reliably determined. It is equally dangerous to use approximation formulae for the parameter esti-

mates, since such an approach ignores the early behavior of the luminosity and expansion velocity, which contain an additional information on the ejecta mass, explosion energy, and pre-SN radius.

Until recently a sensitive point of the hydrodynamic approach was a “manual” composition mixing and density smoothing between the metal core, the helium core, and the hydrogen envelope of a pre-SN star, although that was well constrained by the light curve at the late plateau. The justification for the manual mixing is the inability of 1D hydrodynamics to treat the Rayleigh-Taylor instability and mixing initiated by the shock propagation in the pre-SN. The recent study dedicated to mixing issue on the basis of the 3D RSG explosion (Utrobín et al. 2017) shows that the manual mixing applied earlier in 1D model of SN 1999em (Utrobín 2007) is fully consistent with the mixing produced by the 3D hydrodynamics. At the moment we do not see another way to seriously improve our hydrodynamic model.

Alternatively, the pre-SN luminosity mass could be underestimated. The most apparent reason is that the pre-SN light might be obscured by a dusty CS envelope (Utrobín & Chugai 2008; Smartt et al. 2009). This possibility finds some support in the growing number of SNe IIP with signatures of a confined dense CS envelope in early spectra, e.g., SN 2006bp (Quimby et al. 2007) and SN 2013fs (Yaron et al. 2017). These data indicate a dense CS shell at the radii  $\lesssim 10^{15}$  cm. To illustrate the point, let us estimate possible optical depth of the CS shell of the mass  $M_s$  at the radius  $R_s = 10^{15}$  cm. The equilibrium temperature of the shell for the stellar luminosity of  $3 \times 10^5 L_\odot$ , characteristic of a  $25 M_\odot$  RSG star, is then  $\sim 900$  K, i.e., below the silicate dust condensation temperature (1000 – 1200 K) for the relevant gas pressure. We adopt the standard dust-to-gas ratio of  $10^{-2}$  and the optical properties of a silicate dust (Draine & Lee 1984), which suggest the absorption efficiency  $Q_a = 0.4(a/\lambda)$  for the grain radius  $a$  of about  $10^{-5}$  cm. The optical depth of the CS shell is then  $\tau = 2.2(M_s/10^{-3}M_\odot)(R_s/10^{15}\text{cm})^{-2}(0.8\mu\text{m}/\lambda)$ . The estimate shows that the shell with the mass  $M_s \sim 10^{-3}M_\odot$ , produced by a sensible RSG mass-loss rate, could maintain significant absorption of the pre-SN light.

Another independent progenitor mass estimate for SN 2013ej ( $12 - 15 M_\odot$ ) is obtained from the nebular oxygen doublet [O I] 6300, 6364 Å (Yuan et al. 2016). The accuracy of this method depends on the uncertainty of the adopted density,  $^{56}\text{Ni}$  distribution, and molecules (i.e., CO and SiO) abundance of the O-rich matter. Note that the cooling by molecules is ignored in the current model. Furthermore, the adopted  $^{56}\text{Ni}$  distribution set by centrally concentrated sphere is an oversimplification in the case of SN 2013ej. Therefore, although this analysis of nebular spectra is an interesting alternative approach, there remain uncertainties that cast shadow on the reliability of the progenitor mass estimate.

## ACKNOWLEDGEMENTS

We thank Govinda Dhungana for kindly sending us the spectra of SN 2013ej. The study by N.C. of  $^{56}\text{Ni}$  asymmetry is partially supported by Russian Scientific Foundation grant 16-12-10519.

## REFERENCES

- Baklanov P. V., Blinnikov S. I., Pavlyuk N. N., 2005, *Astronomy Letters*, **31**, 429
- Bersten M. C., Benvenuto O., Hamuy M., 2011, *ApJ*, **729**, 61
- Bose S., et al., 2015, *ApJ*, **806**, 160
- Chakraborti S., et al., 2016, *ApJ*, **817**, 22
- Chugai N. N., 2006, *Astronomy Letters*, **32**, 739
- Chugai N. N., Fabrika S. N., Sholukhova O. N., Goranskij V. P., Abolmasov P. K., Vlasyuk V. V., 2005, *Astronomy Letters*, **31**, 792
- Dalgarno A., Yan M., Liu W., 1999, *ApJS*, **125**, 237
- Dhungana G., et al., 2016, *ApJ*, **822**, 6
- Draine B. T., Lee H. M., 1984, *ApJ*, **285**, 89
- Fesen R. A., Milisavljevic D., 2016, *ApJ*, **818**, 17
- Fransson C., Kozma C., 1993, *ApJ*, **408**, L25
- Fraser M., et al., 2014, *MNRAS*, **439**, L56
- Hanuschik R. W., 1991, in Danziger I. J., Kjaer K., eds, European Southern Observatory Conference and Workshop Proceedings Vol. 37, European Southern Observatory Conference and Workshop Proceedings. p. 237
- Huang F., et al., 2015, *ApJ*, **807**, 59
- Kim M., et al., 2013, Central Bureau Electronic Telegrams, **3606**
- Kozma C., Fransson C., 1992, *ApJ*, **390**, 602
- Kumar B., Pandey S. B., Eswaraiah C., Kawabata K. S., 2016, *MNRAS*, **456**, 3157
- Lee M., et al., 2013, The Astronomer’s Telegram, **5466**
- Mauerhan J. C., et al., 2017, *ApJ*, **834**, 118
- Maund J. R., Smartt S. J., Danziger I. J., 2005, *MNRAS*, **364**, L33
- Morozova V., Piro A. L., Valenti S., 2017, *ApJ*, **838**, 28
- Quimby R. M., Wheeler J. C., Höflich P., Akerlof C. W., Brown P. J., Rykoff E. S., 2007, *ApJ*, **666**, 1093
- Sahu D. K., Anupama G. C., Srividya S., Muneer S., 2006, *MNRAS*, **372**, 1315
- Shappee B. J., et al., 2013, The Astronomer’s Telegram, **5237**
- Smartt S. J., Eldridge J. J., Crockett R. M., Maund J. R., 2009, *MNRAS*, **395**, 1409
- Utrobín V. P., 2004, *Astronomy Letters*, **30**, 293
- Utrobín V. P., 2007, *A&A*, **461**, 233
- Utrobín V. P., Chugai N. N., 2008, *A&A*, **491**, 507
- Utrobín V. P., Chugai N. N., 2009, *A&A*, **506**, 829
- Utrobín V. P., Chugai N. N., 2011, *A&A*, **532**, A100
- Utrobín V. P., Chugai N. N., 2015, *A&A*, **575**, A100
- Utrobín V. P., Wongwathanarat A., Janka H.-T., Müller E., 2017, *ApJ*, **846**, 37
- Wongwathanarat A., Müller E., Janka H.-T., 2015, *A&A*, **577**, A48
- Woosley S. E., 1988, *ApJ*, **330**, 218
- Yaron O., et al., 2017, *Nature Physics*, **13**, 510
- Yuan F., et al., 2016, *MNRAS*, **461**, 2003

This paper has been typeset from a  $\text{\TeX}/\text{\LaTeX}$  file prepared by the author.